Epitaxy on Demand

Maarten Nijland, Sean Thomas, Mark A. Smithers, Nirupam Banerjee, Dave H. A. Blank, Guus Rijnders, Jing Xia, Gertjan Koster, and Johan E. ten Elshof*

Perovskite oxide heteroepitaxy is realized on the top of inorganic nanosheets that are covering the amorphous oxide surfaces of Si substrates. Utilizing pulsed laser deposition, thin films of $SrRuO_3$ in a $(001)_{pc}$ and $(110)_{pc}$ orientation on nanosheets of $Ca_2Nb_3O_{10}$ and $Ti_{0.87}O_2$ are grown, respectively. The two types of nanosheets are patterned to locally tailor the crystallographic orientation and properties of $SrRuO_3$. The success of our approach is demonstrated by electron backscatter diffraction and spatial magnetization maps. An unprecedented control of perovskite film growth on arbitrary substrates is illustrated in this work, and the methods that are developed to deposit $SrRuO_3$ thin films are a viable starting point for growth of artificial heteroepitaxial thin films that require a bottom electrode. Control is not just reached in the direction of film growth, as the crystal orientation and film properties are regulated laterally on the surface of micropatterned nanosheets. Local control of magnetic properties is illustrated, which holds out prospects for the fabrication of next-generation devices like noncollinear magnetic random access memories.

1. Introduction

The past years have seen an inexhaustive interest in complex oxide electronics, which has largely been fueled by the atomic scale precision with which metal oxide thin films can be deposited and the associated phenomena originating from the artificial interfaces, epitaxial stress, and strain, and/or crystallographic orientation.[1–8] Development and commercialization of perovskite-based devices have for a large part been hampered by the challenge to interlace the technology with existing (Si-based) processes, which is related to the requirement for a lattice-matching inert crystal to direct the film formation. The unparalleled control of the crystal structure as can be reached on single-crystalline substrates should not only be retained, but also scaled-down and patterned in order to achieve miniaturization. This requirement also poses enormous challenges for the application of complex oxides in practical devices such as solar cells, sensors, actuators, transistors, and storage media.

The outstanding ferromagnetic properties found in perovskite oxides hold great promise for next-generation magnetic random access memories (MRAMs). Radical miniaturization of MRAMs is expected when electrical currents are exploited to manipulate the magnetization of a ferromagnet, which can be achieved by utilization of the spin angular momenta and resulting spin-transfer torques.[9] Since spin-transfer torques are zero in the case of collinearly magnetized devices, magnetic tunnel junctions with noncollinear magnetization are required to be able to reach sufficient switching speeds.[9,10] Such devices can be fabricated when the crystal structure of a material can be tailored within the dimensions of a memory element, and realizing such control asks for methods to pattern the crystal structure of thin films.

Textured growth of various metal oxide layers on arbitrary substrates was recently illustrated by epitaxy on inorganic nanosheets,[11–17] which by their lateral sizes in the (sub-)μm range and variety of crystal lattices[18] allow for new possibilities to locally tailor the important structural parameters of a thin film. This opportunity is exploited in this work, where we show that we were able to pattern the strain, crystallographic orientation, and properties of a perovskite oxide thin film. Therewith, major restrictions for the design of functional devices are lifted, as this approach allows to locally control the growth and properties of thin films without changing their compositions.

Pulsed laser deposition (PLD) was used to form thin films of $SrRuO_3$ on silicon substrates with amorphous oxide surfaces, during which two different kinds of nanosheets were used to orchestrate crystal growth: Crystalline templates of $Ca_2Nb_3O_{10}$ led to epitaxial growth in the $[001]_{pc}$ direction, while seed layers of $Ti_{0.87}O_2$ yielded $(110)_{pc}$ oriented films; label pc refers to a pseudo-cubic crystal symmetry. We stress that in both of these cases, the films of $SrRuO_3$ were epitaxial with respect to the underlying nanosheets, so no structural coherency with the lattice of the silicon substrate was realized. Being ferromagnetic typically below ≈160 K,[19] the conducting perovskite was deposited not only to illustrate the ability to locally tune its magnetic behavior, but also because of its widespread application as electrode in all oxide heterostructures.[20] Results on growth of this material on substrates covered exclusively with nanosheets of either $Ca_2Nb_3O_{10}$ or $Ti_{0.87}O_2$ are discussed first, and the purpose of these studies was to comprehend and improve growth on the individual nanosheets. Several ways are introduced to

Dr. M. Nijland, M. A. Smithers, Dr. N. Banerjee, Prof. D. H. A. Blank, Prof. G. Rijnders, Prof. G. Koster, Prof. J. E. ten Elshof
MESA+ Institute for Nanotechnology
University of Twente, P.O. Box 217
7500 AE, Enschede, The Netherlands
E-mail: g.koster@utwente.nl
S. Thomas, Prof. J. Xia
Department of Physics and Astronomy
University of California
4129 Frederick Reines Hall, Irvine, CA 92697-4575, USA

DOI: 10.1002/adfm.201501483

master film growth on top of the 2D seed crystals, which led to thin films of $SrRuO_3$ that showed strong resemblance to fully oriented ones when, e.g., roughnesses or resistivities were compared. The properties of the films are shown to depend on the underlying nanosheets, and by fabricating micropatterns of both types of nanosheets, these properties were combined into a single sample. For instance, we show that we are able to control the rotation of the magnetic easy axis in our films, taking a step in the direction of next-generation MRAMs.

2. Results and Discussion

2.1. Atomically Smooth Growth of $SrRuO_3$ on Nanosheets of $Ca_2Nb_3O_{10}$

Nanosheets were transferred onto Si substrates by Langmuir–Blodgett depositions, after which atomic force microscopy (AFM) was used to confirm successful formation of dense monolayers. An example of a resulting image is given in **Figure 1**a, in which single nanosheets can be recognized that collectively formed a closely packed film, of which only a minor part consisted of overlapping or stacked sheets. Based on AFM images recorded at six random locations, the coverage of nanosheets on this sample was determined to be 95 ± 2%.

Utilizing reflection high energy electron diffraction (RHEED) during subsequent PLD of $SrTiO_3$ and $SrRuO_3$, growth was monitored in situ by measuring the intensity and full width at half maximum (FWHM) of the specular spot. It developed from a faint elongated spot before growth (**Figure 2**a) into a spot of much higher intensity, which remained clearly visible during the entire depositions of both $SrTiO_3$ (Figure 2b) and $SrRuO_3$. As shown in Figure 2c and observed in all of the experiments performed, the intensity of the specular spot dipped during deposition of the first one or two monolayers of $SrTiO_3$, after which it sharply increased and started to oscillate while it further increased steadily.

The low intensity of the RHEED specular spot observed before growth can be explained by the small number of crystal planes in the nanosheets. During the first few pulses of $SrTiO_3$, the intensity of the specular spot dropped even further due to increased scattering of the electrons from the coarsened surface. Continuation of growth led to formation of additional crystal planes from which the electrons could diffract, causing the (sharp) increase of intensity. Most importantly though, oscillations were observed which are a footprint of atomic layer-by-layer growth and enable monitoring and controlling thin film growth on the atomic level. Note that similar observations have only been reported on lattice-matching single-crystalline substrates, while in this case epitaxial registry with the substrate was absent.

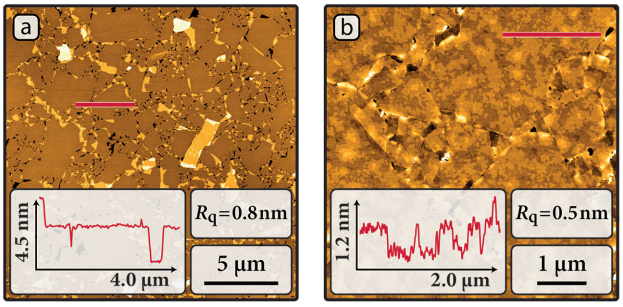

Figure 1. Tapping mode AFM height images of a) a layer of $Ca_2Nb_3O_{10}$ nanosheets on Si measured directly after Langmuir–Blodgett deposition and b) the same sample after PLD of $SrTiO_3$ and $SrRuO_3$. The insets show height profiles measured along the (red) lines in the corresponding images and values for the root mean square roughness (R_q) are given as well.

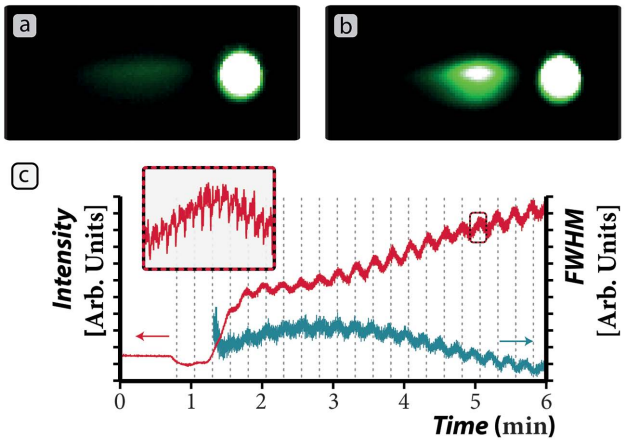

Figure 2. RHEED images a) before and b) after growth of $SrTiO_3$ together with c) the evolution of specular spot intensity (red) and full width at half maximum (FWHM; blue) during initial growth of $SrTiO_3$ (the inset is a magnification of a single oscillation).

The sample is referred to as sample 1 (see **Table 1**), and was analyzed by X-ray reflectivity (XRR) and X-ray diffraction (XRD). Resulting values for the thicknesses (t), roughnesses (R), and out-of-plane lattice parameters (d) of both the $SrTiO_3$ and $SrRuO_3$ layers are given in **Table 2**. Sample 2 was made for reference, which comprised a thin film of $SrRuO_3$ that was deposited under similar conditions on a $(001)_c$ oriented single-crystalline substrate of $SrTiO_3$. Table 2 also includes values for t, R, and d obtained for sample 2.

In the 2θ–ω scan of **Figure 3**a, all peaks could be assigned either to the $(00l)_{c/pc}$ planes of the perovskite oxide layers

Table 1. List of samples studied in this work, schematical representations of samples 1, 3, and 5 can be found in the Supporting Information.

Sample	Stack
1	Si $(100)_c$ substrate with thermal oxide | one layer of $Ca_2Nb_3O_{10}$ nanosheets | $SrTiO_3$ $(001)_c$ | $SrRuO_3$ $(001)_{pc}$
2	$SrTiO_3$ $(001)_c$ substrate | $SrRuO_3$ $(001)_{pc}$
3	Si $(100)_c$ substrate with thermal oxide | two layers of $Ti_{0.87}O_2$ nanosheets | $SrTiO_3$ $(110)_c$ | $SrRuO_3$ $(110)_{pc}$
4	$SrTiO_3$ $(110)_c$ substrate | $SrRuO_3$ $(110)_{pc}$
5	Si $(100)_c$ substrate with thermal oxide | one layer of $Ti_{0.87}O_2$ nanosheets | $SrTiO_3$ $(110)_c$ | $SrRuO_3$ $(110)_{pc}$
6	Si $(100)_c$ substrate with thermal oxide | two layers of $Ti_{0.87}O_2$ nanosheets | line pattern of $Ca_2Nb_3O_{10}$ nanosheets | $SrTiO_3$ line pattern alternating between $(110)_c$ and $(001)_c$ | $SrRuO_3$ line pattern alternating between $(110)_{pc}$ and $(001)_{pc}$

Table 2. Values obtained from XRD analyses and magnetic and electrical characterizations of samples 1–4 (see Table 1). Values for the layer thickness (t) and roughness (R) were determined by XRR, and the out-of-plane lattice parameters (d) were determined from 2θ–ω scans. The number in brackets behind every value is the error of the last digit to fall within a certainty of 95%. The characterization part includes values for the absolute saturation magnetization ($M_{s,abs}$), Curie temperature (T_C), magnetic anisotropy, sheet resistivity at 300 K (ρ_{300K}), and the residual resistivity ratio (ρ_{300K}/ρ_{5K}). A value for the magnetic anisotropy was obtained by dividing the out-of- plane remnant magnetization ($M_{R,\perp}$) by the in-plane component ($M_{R,\parallel}$) within a temperature range of $T = 10$ K to $T = T_C - 10$ K (the value was found independent of T).

Sample	Layer	Analysis			Characterization				
		t [nm]	R [nm]	d [Å]	$M_{s,abs}$ [μ_B/Ru]	T_C [K]	$M_{R,\perp}/M_{R,\parallel}$	ρ_{300K} [$\mu\Omega$ cm^{-1}]	ρ_{300K}/ρ_{5K}
1	$SrRuO_3$ $(001)_{pc}$ $SrTiO_3$ $(001)_c$	14.5(1) 17.2(3)	0.67(3) 0.5(2)	3.942(4) 3.915(7)	1.05	137	2.0(3)	360	2.6
2	$SrRuO_3$ $(001)_{pc}$	14.1(3)	0.23(4)	3.96(1)	1.20	125	3.2(4)	322	2.7
3	$SrRuO_3$ $(110)_{pc}$ $SrTiO_3$ $(110)_c$	13(1) 18.3(5)	3.1(3) 1.1(5)	3.925(8) 3.908(3)	1.04	155	0.7(1)	358	3.7
4	$SrRuO_3$ $(110)_{pc}$	14(2)	4.2(7)	3.958(3)[a]	1.47	154	7.7(6)	318	5.9

[a]XRD data indicate that most of the film is completely strained to the substrate and that a minor part is relaxed (see reciprocal space maps in the Supporting Information). The out-of-plane lattice parameter in this table corresponds to the strained part.

or of the Si substrate. The out-of-plane lattice parameters indicate that at least the layer of $SrRuO_3$ was compressively strained on the $SrTiO_3$ buffer layer. The lattice spacing of the interlayer of $SrTiO_3$ was also larger than that of bulk $SrTiO_3$, but the obtained value does not necessarily signify that the buffer layer was compressively strained. Film peaks were found when similar growth conditions were used to deposit $SrTiO_3$ on a single-crystalline substrate of $SrTiO_3$, suggesting that the increased lattice parameter may just as well have resulted from off-stoichiometric growth. Clear Laue oscillations were observed around the $(001)_{c/pc}$ diffraction spots (Figure 3b), the periodicities of which corresponded well with the thicknesses of the two layers as determined from XRR.

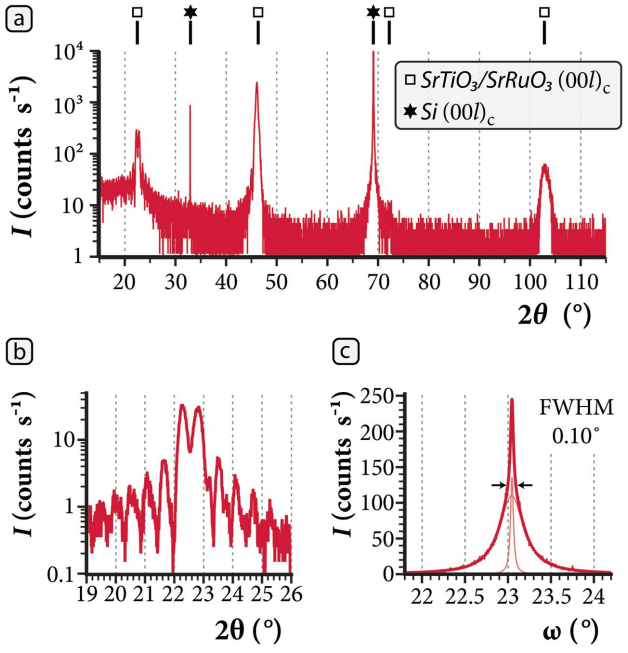

Figure 3. XRD patterns of sample 1 (see Table 1), showing results from a,b) 2θ–ω scans, and c) ω-rocking around $2\theta = 46.08°$. The pattern in image (b) was recorded using a triple axis module, and the rocking curve in (c) is displayed together with fits to two Lorentzian functions.

A strong preferential orientation of the layers was confirmed from ω-rocking scans around the $(002)_{c/pc}$ peaks assigned to $SrTiO_3$ (at $2\theta = 46.47°$) and $SrRuO_3$ (at $2\theta = 46.08°$); the latter rocking curve can be found in Figure 3c. The rocking curves were best fitted with two Lorentzian functions having a combined FWHM of 0.10°, which is to our knowledge the smallest ever reported for a film on nanosheets. Still, the spread of crystal orientations is larger than that measured for the film of $SrRuO_3$ deposited on a $(001)_c$ oriented $SrTiO_3$ substrate (FWHM = 0.03°). The fact that the film peaks could exclusively be assigned to the $(00l)_{c/pc}$ planes and the strong texture that was observed in the rocking curves indicate that both layers of $SrTiO_3$ and $SrRuO_3$ were epitaxially coupled to the underlying nanosheets.

Figure 1b shows an AFM image of sample 1 after growth of the $SrTiO_3$ and $SrRuO_3$ heterostructure. Our films grown on $Ca_2Nb_3O_{10}$ nanosheets were almost as smooth as those deposited on single crystalline $(001)_c$ oriented $SrTiO_3$ substrates, and even atomic terraces were observed, as also illustrated by the height profile in Figure 1b. Growth clearly benefited from the presence of the interlayer of $SrTiO_3$, since islands of $SrRuO_3$ were obtained when the buffer layer was excluded. The reason for the strong influence of the buffer layer on the morphology of $SrRuO_3$ may be twofold: The newly created interfaces lead to alteration of the interfacial energies and chemistries, which influences growth kinetics of $SrRuO_3$; and epitaxial strain may be released in the interlayer, which leads to slower evolution of stress during epitaxial growth of the conducting perovskite. To distinguish between these two possible causes, the effect of reducing the thickness of the interlayer on the morphology of the films of $SrRuO_3$ was studied ex situ (AFM images can be found in the Supporting Information). These studies showed that the first unit cells of $SrTiO_3$ played a crucial role in the formation of islands during deposition of $SrRuO_3$, since only four to six unit cells were required to obtain smooth films of $SrRuO_3$. Smooth interlayers were obtained in every case, and the AFM data indicate that three unit cells were sufficient to completely cover the surfaces of the nanosheets by $SrTiO_3$. Still, nucleation of islands was not completely suppressed in this case, which suggests that island formation may not be solely due to interfacial effects. Any interdiffusion between

components of the nanosheets and interlayer during deposition of the initial unit cells of $SrTiO_3$ can not be excluded though.

The other hypothesis to explain the effect of the buffer layer, namely that the initially large lattice mismatch between $SrRuO_3$ and the nanosheets (+1.7%) was reduced by the introduction of an interlayer of $SrTiO_3$, remains plausible. Since the roughness of the $SrRuO_3$ thin film was determined by the first unit cells of the buffer layer, this hypothesis requires that elastic strain was relieved in the first few atomic layers of $SrTiO_3$. Relaxation of the buffer layer may have resulted from formation of dislocations to reduce stress caused by lattice matching with the nanosheets, but may also be explained by transfer of strain into the nanosheets. The latter option considers the nanosheets to be flexible as a result of their 2D nature,[14, 16] but requires them to be attached to the substrate by weak (nondirectional) interactions only during PLD of the initial atomic layers. When a film with larger lattice parameters than that of the nanosheets is grown (like in the present case), sufficient space should be available for the nanosheets to allow their lateral expansion. Considering the dense packing of nanosheets in our case, large atomic displacements in the nanosheets could have been obstructed with the result that generation of defects in the film was inevitable.

Since $SrRuO_3$ is a good conductor and possesses large magnetocrystalline anisotropy that is highly sensitive to its condition in a thin film, the material has served as an electrode in various perovskite heterostructures, and has evolved as a model system for studying magnetism.[20] Here, magnetic and electrical properties were studied to evaluate the applicability of the film as a conducting layer, and to understand how properties are determined by the seed layer, putting sample 1 in perspective with the fully oriented sample 2.

Figure 4a shows magnetic hysteresis loops of sample 1, measured at 10 K for the in-plane (blue squares) and out-of-plane (red circles) directions. In both cases a coercive field of H_c = 0.8×10^6 A m^{-1} was measured, and the easy axis was found to be pointing out of the surface plane. The temperature dependence of saturation and remnant magnetization measured along the easy direction is shown in Figure 4b, and includes the best result from fits of the saturation magnetization with Brillouin functions for different total angular momentum quantum numbers (J). The best fit was obtained for the Langevin functional dependency ($J = \infty$), yielding an absolute saturation magnetization and Curie temperature as given in Table 2. A value for the anisotropy was obtained by taking the ratio of the out-of-plane and in-plane remnant magnetization ($M_{R,\perp}/M_{R,\parallel}$), which was found constant within a temperature range of $T = 10$ K to $T = T_C - 10$ K. Table 2 also includes values for the room temperature resistivity and residual resistivity ratio obtained from the graph displayed in Figure 4c. Values resulting from magnetic and electrical characterization of sample 2 are also included in Table 2.

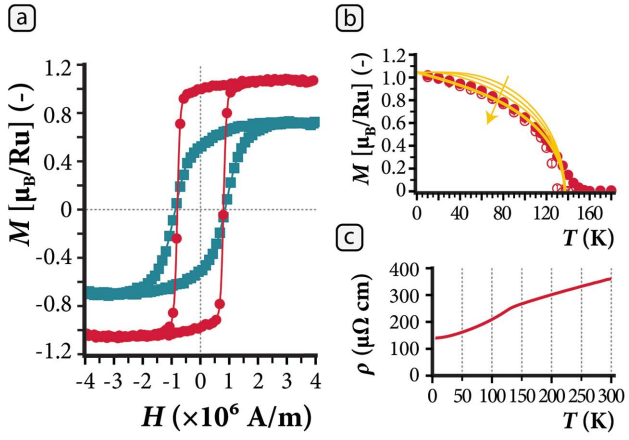

Figure 4. Magnetic and electrical characterization of sample 1 (see Table 1). a) Magnetic hysteresis curves obtained at 10 K measured with the field applied in the surface plane (blue squares) and out-of-plane (red circles). b) Temperature dependence of saturation magnetization (closed circles) and remnant magnetization (open circles) for the out-of-plane direction, together with Brillouin curves (in yellow) from Weiss theory of ferromagnetism for different total angular momentum quantum numbers $J = 1, 2, 4, \infty$, where J increases in the direction of the arrow (the best fit is displayed in bold, the other curves use the values of the absolute saturation magnetization and Curie temperature obtained from the best fit). c) Sheet resistivity (ρ) plotted versus temperature.

Clear magnetic anisotropy was observed together with a Curie temperature of T_C = 137 K. The Curie temperature of sample 1 was significantly lower than that of bulk $SrRuO_3$, for which $T_C \approx 160$ K.[19] The reduced Curie temperature was probably the result of strain in the layer of $SrRuO_3$, as strain is known to affect both electrical and magnetic properties of the material.[21,22] An even lower Curie temperature was observed in the film on $(001)_c$ oriented $SrTiO_3$ (see Table 2 and Supporting Information). This observation indicates that $SrRuO_3$ experienced more strain from the single crystal than from the buffer layer on nanosheets, which is in accordance with the out-of-plane lattice parameters (see Table 2). Variation of stoichiometry between the single crystal and buffer layer may explain the different amounts of strain between the two films of $SrRuO_3$. In addition, imperfections existing in the interlayer may affect growth of $SrRuO_3$, and lead to partial relaxation of strain.

Upon further comparing the magnetic properties of the fully oriented film and the film on nanosheets, a stronger anisotropy was found in the former case (see Table 2). Full comparison between the two samples in this context is not meaningful, since one sample had a single crystallographic orientation while the other had an orientation that was only fixed in the out-of-plane direction. Still, this difference may be explained by unequal strain states between the two films, as strain has a strong influence on anisotropy in films of $SrRuO_3$.[22] Another difference between the two samples is that Brillouin fits suggest classical behavior ($J = \infty$) of the spins in $SrRuO_3$ on nanosheets, while partial quantization of the angular momentum ($J = 4$) is indicated for the fully oriented film. This difference is possibly the result of the slightly higher out-of-plane crystallographic order in the film on the $SrTiO_3$ substrate, resulting in detection of quantization only in this case.

While the crystal structure of sample 2 was fully dictated by the single-crystalline $SrTiO_3$ substrate, sample 1 was not fully oriented as no heteroepitaxy with the Si substrate was reached. Nevertheless, the resistivity of sample 1 was only slightly higher than that of sample 2, and residual resistivity ratios were comparable. In combination with the atomic scale roughness and well-controlled crystal structure, these results reveal the potential of using nanosheets to prepare artificial epitaxial heterostructures with $SrRuO_3$ bottom-electrodes, as nanosheets offer

a high degree of control during PLD and remove the restriction of having to use specific substrates with matching lattice parameters.

2.2. Optimized Growth of $SrRuO_3$ on Two Layers of $Ti_{0.87}O_2$ Nanosheets

To make sample 3, two consecutive Langmuir–Blodgett depositions were performed to coat a Si substrate with two layers of $Ti_{0.87}O_2$ nanosheets, of which the first layer covered 97.7 ± 0.8% of the substrate, and the second layer covered 94.8 ± 0.9% of that surface. An AFM image recorded after deposition of the second layer is shown in **Figure 5**a, where the height profile in the inset was obtained at one of the rare locations where the substrate was still exposed, and clearly reveals the two layers of nanosheets. The AFM image of Figure 5b was measured after PLD of $SrTiO_3$ and $SrRuO_3$, and shows that the surface morphology had coarsened by formation of sub-100 nm grains. Table 2 contains values resulting from XRR and XRD analyses of this sample and a fully $(110)_{pc}$ oriented film of $SrRuO_3$ that was deposited under similar conditions on a single-crystalline $(110)_c$ $SrTiO_3$ substrate. The latter sample is referred to as sample 4.

Figure 6 shows XRD patterns of two samples where $SrTiO_3$ and $SrRuO_3$ were deposited under similar conditions, but on substrates that were covered by either one or two layers of $Ti_{0.87}O_2$ nanosheets. When just a single layer of nanosheets was used (covering 97.3 ± 0.2% of the substrate), undesired crystallographic orientations were observed, which could not be suppressed by changing the PLD growth temperature between 650 °C and 800 °C. Using a second layer of nanosheets led to complete suppression of undesired orientations and an over tenfold increase of the peak intensities of the preferred (*hh*0) orientation, which is even more significant when considering that the monolayer of nanosheets consisted for 5 ± 1% of overlaps and stacks. Probably, the second layer of nanosheets was required because at elevated temperatures the first layer reacted with the substrate and underwent partial structural transformations, impeding epitaxial growth of the perovskite film. These transformations did not involve long-range migrations of atoms, since no significant morphological changes were observed by AFM before and after heating a Si substrate containing a single layer of $Ti_{0.87}O_2$ nanosheets. Based on analysis by X-ray photoelectron spectroscopy (XPS; Supporting Information), we conclude that the first layer of nanosheets may have been prone to formation of titanium silicates by reaction with the amorphous silicon oxide surface, provoked by the direct contact between the two.

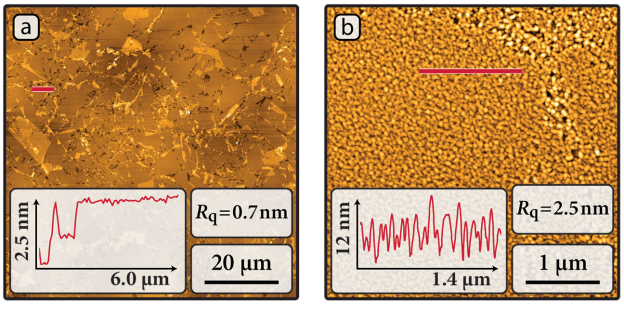

Figure 5. AFM height images of $Ti_{0.87}O_2$ nanosheets on Si a) after the second Langmuir–Blodgett deposition and b) after PLD of $SrTiO_3$ and $SrRuO_3$. Both images include a value for the roughness (R_q) and a height profile measured along the (red) line in the corresponding image.

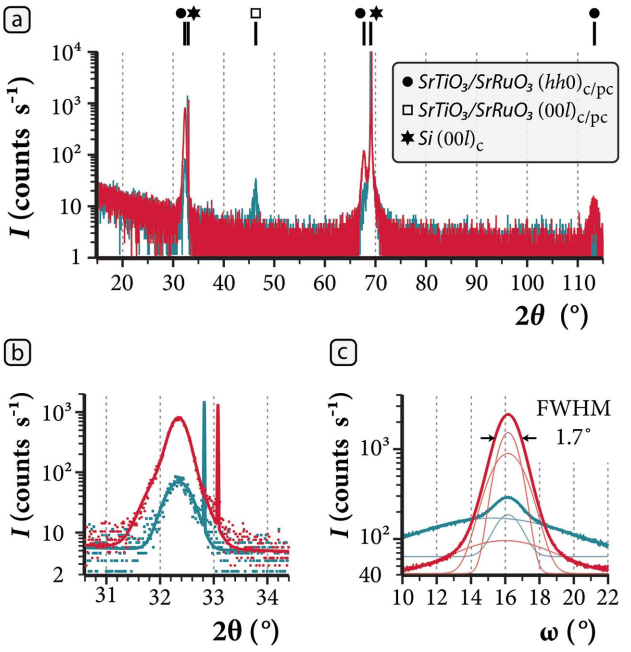

Figure 6. XRD patterns of sample 3 and sample 5 (see Table 1), including results from a,b) 2θ–ω scans and c) rocking ω around 2θ = 32.35°. The red curves (the ones that show highest intensity around 2θ = 32.35°) were obtained on sample 3, the blue curves were acquired from sample 5. The curve in image (b) was fitted to three Gaussian functions, where one was used to fit the peak of the Si substrate, and two to fit those of the film. The ω-rocking curves in image (c) are displayed together with Gaussian fits that were used to determine the FWHM (the value for the FWHM applies to both rocking curves).

Using two layers of $Ti_{0.87}O_2$ nanosheets instead of one did not only influence the crystallographic orientation, but also resulted in a smoother film (the roughness of sample 5 was R_q = 3.9 nm). Still, sample 3 was significantly rougher than those discussed in the preceding section, which is attributed to the high surface energy of the $(110)_{pc}$ planes of $SrRuO_3$.[15] The roughness of $SrRuO_3$ on two layers of nanosheets (sample 3) was similar to that of the film deposited on a $(110)_c$ oriented single-crystalline $SrTiO_3$ substrate (sample 4). Crystallographically these two films differed to a greater extent, since XRD studies on sample 4 indicated partial preservation of strain, as well as a smaller angular spread of the crystallographic orientation (rocking ω around $(110)_{pc}$ yielded a FWHM of 0.04°). Substantial lattice mismatch between the perovskite layers and $Ti_{0.87}O_2$ nanosheets lies at the basis of the reduced control of crystallographic orientation, and the absence of strain in these films.

Magnetic and electrical characterization was performed on sample 3, of which the results can be found in **Figure 7** and Table 2. Comparing the hysteresis curves measured in the two directions, almost equal coercivities (H_c = 1.0 to 1.1 × 10^6 A m^{-1}) but different saturation and remnant magnetization were

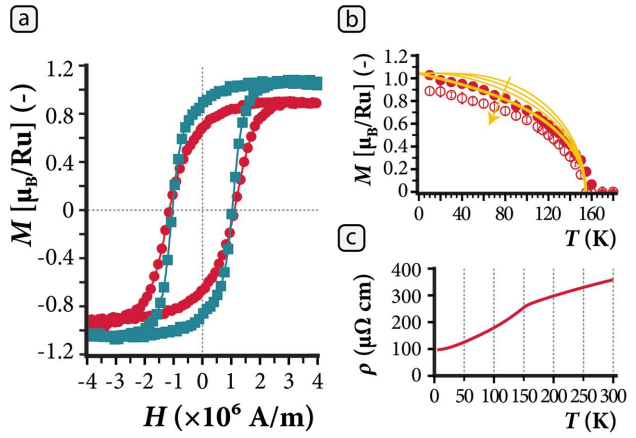

Figure 7. Magnetic and electrical characterization of sample 3 (see Table 1). Magnetic characterization includes a) hysteresis curves measured at 10 K for the in-plane (blue squares) and out-of-plane (red circles) directions and b) temperature dependence of saturation magnetization (closed circles) and remnant magnetization (open circles) when the field was applied in-plane. Similar as in Figure 4, Brillouin curves are displayed that resulted from the best fit (indicating $J = \infty$). Electrical characterization includes c) the sheet resistivity of the sample plotted versus temperature.

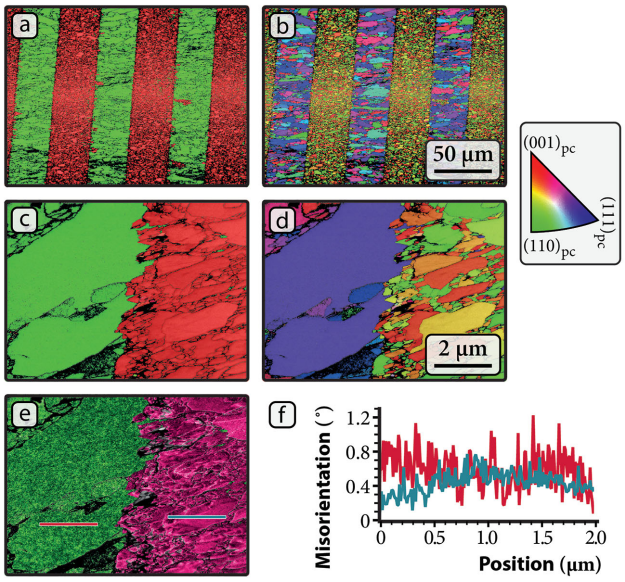

Figure 8. Inverse pole figure maps at a,b) low (step size of 300 nm) and c,d) high (step size of 10 nm) magnification measured by electron backscatter diffraction (EBSD) on sample 6 (see Table 1). For both magnifications, the orientation of the film is displayed from a,c) the out-of-plane and b,d) an in-plane perspective. e) Out-of-plane texture map of the $(110)_{pc}$ and $(001)_{pc}$ oriented grains using a green and purple color gradient, respectively (both maps cover a total misorientation range of 1.5°). f) Misorientation profiles measured along the lines in the texture map (the color of the profiles and the lines along which they were measured are equivalent). The inverse pole figure maps are overlayed on the band contrast image whereas in the case of the texture map, the band contrast image is displayed only for the locations without solution. All maps are viewed as measured, without application of any form of noise reduction.

measured, which showed highest values when the field was applied in the surface plane. Compared to the film on $Ca_2Nb_3O_{10}$ nanosheets, the easy axis pointed in a different direction and the anisotropy appeared weaker (Table 2). The latter observation can be explained by considering that the easy axis of the film on $Ti_{0.87}O_2$ nanosheets did have an in-plane component, meaning that the magnetostatic energy could never be completely minimized (since the in-plane orientation of the nanosheets could not be controlled). Evidently, the magnetic properties of the film on $Ti_{0.87}O_2$ nanosheets were different from those on $Ca_2Nb_3O_{10}$ nanosheets, illustrating the ability to manage material properties by using lattice matching nanosheets.

In contrast to sample 3, the easy axis of the $SrRuO_3$ thin film of sample 4 was pointing out-of-plane (Supporting Information). Rotation of the easy axis can be explained by differences in strain between the two films, as Jung and co-workers illustrated that the magnetic anisotropy and direction of the easy axis in films of $(110)_{pc}$ oriented $SrRuO_3$ changed under the act of strain engineering.[23] Another difference between sample 3 and sample 4 is that in the former case no signs of quantization of the magnetic spins were observed, while in the latter case $J = 4$ was found. In addition, although the room temperature resistivities of the two samples were of the same order of magnitude, values diverged when the temperature was reduced, as clearly reflected by the higher residual resistivity ratio of sample 4 (Table 2). These differences possibly originate from the inferior crystallographic order of the film on nanosheets, as reflected by its multitude of grain boundaries and poorer film texture.

2.3. Films of $SrRuO_3$ with Micropatterned Orientations

The preceding discussion illustrates the potential of nanosheets to control crystal nucleation, which provides an entirely new toolbox to locally tune the structural parameters and properties of thin films. To illustrate this concept, $Ca_2Nb_3O_{10}$ nanosheets were micropatterned on the top of two layers of $Ti_{0.87}O_2$ and used to locally tailor the orientation of $SrRuO_3$, yielding sample 6. Crystallographic information of this film was obtained by electron backscatter diffraction (EBSD) (see **Figure 8**). The inverse pole figure maps in this figure indisputably prove the ability to control the crystal structure, since line patterns altering between an $(001)_{pc}$ and $(110)_{pc}$ orientation can clearly be recognized. Strong proof for epitaxy can be found in the maps containing the in-plane crystallographic information, in which the shapes and sizes of the different domains corresponded to those of the nanosheets.

A texture map showing misorientation from the ideal $[001]_{pc}$ and $[110]_{pc}$ directions is found in Figure 8e, from which clear differences in microtexture can be observed that are directly related to the control of crystal nucleation and growth that was achieved on the two types of nanosheets. The $(110)_{pc}$ oriented part consisted of small subgrains that did not show any mutual correlation, which was caused by the significant mismatch between $Ti_{0.87}O_2$ and the perovskite film. In contrast, a more gradual change of orientation was indicated on the $(001)_{pc}$ oriented film and intra-grain boundaries were observed in some of the (larger) domains. Note for instance the misorientation profile in Figure 8f that was made along a single $(001)_{pc}$ oriented domain, which indicates coexistence of two subgrains having

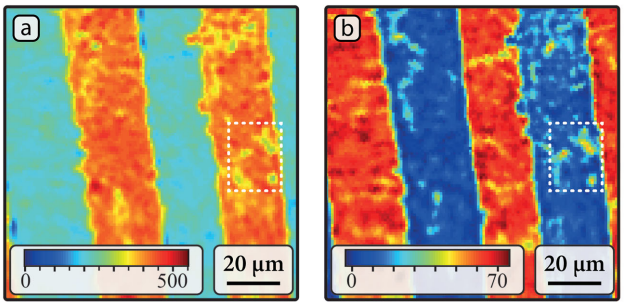

Figure 9. Spatial Kerr signal of sample 6 (see Table 1) obtained by optical magnetometry at a) 78 K and b) 135 K. The sample was cooled from room temperature to 78 K in a perpendicular field of 0.16×10^6 A m^{-1}, the polar magneto-optic Kerr effect (MOKE) was measured in zero field. The sample was heated in zero field between the two measurements. The values on the color scales are in µrad, and both map scans show the same area.

a boundary approximately halfway. This kind of microtexture may have originated from imperfections in the seed layer, like undulations or cracks of the nanosheets, but may have also developed during relaxation events.

The spatial Kerr maps in **Figure 9** demonstrate that patterning of the orientations allowed local tuning of the magnetic characteristics of the film. At 78 K, the complete film was ferromagnetic and the $(001)_{pc}$ oriented lines showed highest magnetization of the two. Upon increasing the temperature, half of the material could be rendered paramagnetic, while the other $(110)_{pc}$ oriented half remained ferromagnetic until $T_C \approx$ 150 K. These observations are corresponding with the measurements performed on the unpatterned thin films. For instance, dissimilar Curie temperatures were measured for the film on $Ca_2Nb_3O_{10}$ and $Ti_{0.87}O_2$ nanosheets (see Table 2). As most markedly recognized in the area enclosed by the dashed box, the paramagnetic lines still contained traces of ferromagnetic material. These erratic features shared their Curie temperature with the $(110)_{pc}$ oriented lines, and appeared at the same location and with the same shape at 78 K by showing a lower magnetization than their surrounding. These observations strongly indicate that these regions actually contained $SrRuO_3$ oriented in the $[110]_{pc}$ direction. Such deviations from the intended crystal orientation may have resulted from an incomplete coverage of $Ca_2Nb_3O_{10}$ nanosheets, as can also be discerned in the EBSD images. Note that the spot size of the modified Sagnac interferometer corresponded to ≈2 µm, implying that the ferromagnetic features may appear larger than they actually were. Considering the overall picture, the magnetic characteristics of the patterned lines are matching well with those measured for the two thin films discussed in the previous sections, indicating that the deposition was not influenced by the act of patterning.

In the foregoing paragraphs, line patterns with periodicities of several tens of micrometers were discussed. Further reduction of the dimensions of these patterns is desired, but limited by the dimensions of the nanosheets (the nanosheets should be at least smaller than the dimensions of the photoresist pattern as they have to fit in the recessed areas). Note that $Ca_2Nb_3O_{10}$ nanosheets were patterned because of their smaller dimensions compared to $Ti_{0.87}O_2$ nanosheets. No attempts were made to further decrease the pattern dimensions, but we propose that miniaturization is possible either by reducing the dimensions of the nanosheets or by pursuing a top-down approach to make the patterns. To reduce the dimensions of the nanosheets, either the solid-state syntheses of the precursor powders should be controlled to promote nucleation and inhibit growth of the crystals, or the powders should be ground after their syntheses. If a top-down approach is developed (where one type of nanosheets is selectively etched), the size of the nanosheets will no longer be a critical parameter for the size of the patterns.

3. Conclusion

Perovskite oxide thin films were deposited on Si substrates covered with inorganic nanosheets of $Ca_2Nb_3O_{10}$ or $Ti_{0.87}O_2$. These nanosheets were used as crystalline templates to control the nucleation of the films, which consisted of a $SrTiO_3$ buffer layer and a $SrRuO_3$ top layer. Films were $(001)_{pc}$ oriented on $Ca_2Nb_3O_{10}$ nanosheets, and $(110)_{pc}$ oriented on $Ti_{0.87}O_2$ nanosheets. Micropatterns of $Ca_2Nb_3O_{10}$ were fabricated on two layers of $Ti_{0.87}O_2$ nanosheets, which allowed us to locally control the structure and properties of a perovskite thin film. We were capable of locally tailoring the magnetic properties of our films, introducing noncollinear magnetic patterns, which are essential for next generation MRAM devices.

Inorganic nanosheets can act as templates for growth of heteroepitaxial thin films on substrates that are unsuited for epitaxy by themselves. They allow to control the morphology, crystal structure, and properties of films to a nearly similar extent as can be achieved on lattice-matching substrates. Their tunable lateral sizes and variable lattice parameters offer completely new pathways to tailor nucleation and growth on micrometer length scales. The control of topography, crystal structure, and properties illustrated in this work may serve as foundation for prospective work on all oxide heterostructures, as the atomically smooth thin films of $SrRuO_3$ are ideally suited for bottom electrodes. Besides, the whole new degree of freedom to locally tune the structural parameters, as illustrated by patterning the orientation of $SrRuO_3$ thin films, may have important implications in the design and realization of electronic or electromechanical devices, like storage media, actuators, and sensors.

4. Experimental Section

Patterning of Nanosheets: Slightly deviating from the methods described in previous studies,[24,25] precursor powders were synthesized and exfoliated into unilamellar nanosheets. A detailed experimental procedure can be found in the Supporting Information, which also includes an experimental description of the subsequent Langmuir–Blodgett depositions. To make alternating line patterns of $Ca_2Nb_3O_{10}$ and $Ti_{0.87}O_2$ nanosheets, first two monolayers of $Ti_{0.87}O_2$ nanosheets were deposited and annealed (**Figure 10**a). On top of this sample, hexamethyldisiloxane (Merck) was spin coated first (at 4000 rpm for 45 s), followed by casting a 1.7 µm thick layer of photoresist (OiR 907-12 from Olin Microelectronic Materials Inc.; spin coated at 4000 rpm for 30 s) and heating at 90 °C for 2 min. The sample was then optically exposed (in a Karl Suss MA56 Mask Aligner for 10 s with a Hg lamp emitting at wavelength $\nu = 365$ nm and yielding a surface power density $I = 10$ mW cm^{-2}) under a mask containing various line gratings ranging from 2 to 50 µm in width. The photoresist was subsequently developed

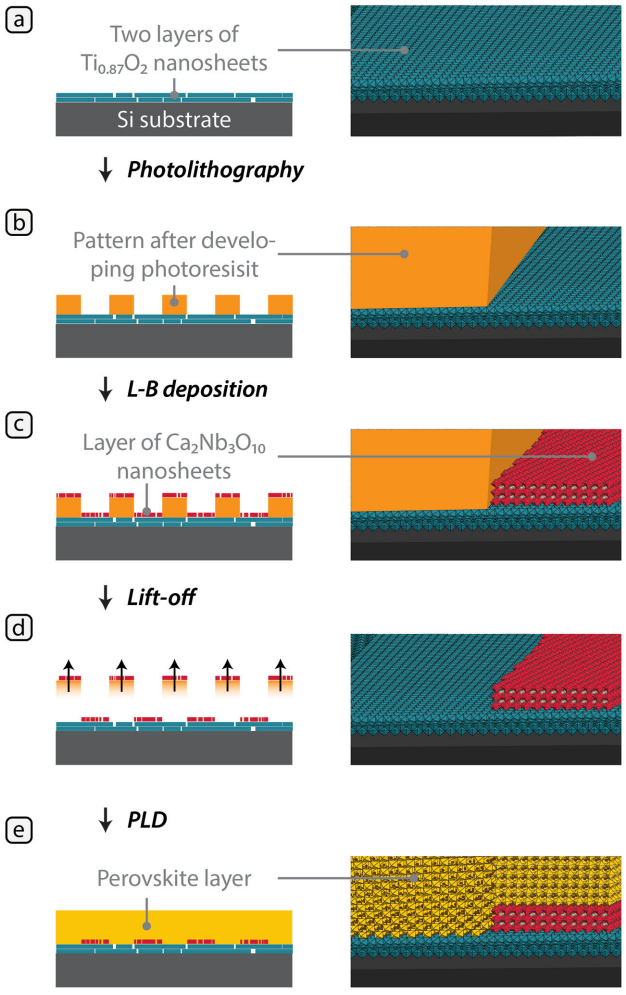

Figure 10. Schematic (left) side view and (right) 3D view of the method that was used to pattern the orientation of a perovskite thin film on an arbitrary substrate. a) Two layers of $Ti_{0.87}O_2$ nanosheets are transferred to the substrate by two sequential Langmuir–Blodgett depositions. b) Then, photolithography is used to pattern photoresist on top of the nanosheets. c) An additional layer of $Ca_2Nb_3O_{10}$ is added by Langmuir–Blodgett deposition and d) the micropattern of photoresist is removed by dissolution in acetone. e) Finally, PLD is used to grow an epitaxial thin film on top of the pattern of nanosheets.

(for 1 min using OPD 4262 from Arch Chemicals) and baked on a hot plate at 110 °C for 2 min (Figure 10b). Prior to the Langmuir–Blodgett deposition of a layer of $Ca_2Nb_3O_{10}$ nanosheets, the patterned sample was treated with a plasma of oxygen (at 30 W for 2 min; Harrick plasma). After the deposition (Figure 10c), the sample was held upside-down in a beaker containing acetone, carefully moved back and forth for 1 min, dipped in and then rinsed with ethanol and finally dried in a stream of N_2 (Figure 10d). HR-SEM images of the resulting pattern can be found in the Supporting Information, which demonstrate the success of patterning.

Pulsed Laser Deposition of $SrTiO_3$ and $SrRuO_3$: Pulsed laser depositions were carried out in a vacuum system equipped with high-pressure RHEED (TSST, the Netherlands) and using a KrF excimer laser (LPXpro from Coherent Inc.; operated at 21.5 kV and ν = 248 nm). The central part of the laser beam was selected with a mask (rectangular shaped with rounded corners and an aperture of 56 mm^2) and focused on the target of choice to a spot size of 1.8 mm^2. The laser output was controlled with a variable attenuator to yield a fluence of 1.30 J cm^{-2} or 2.10 J cm^{-2} on the stoichiometric targets of $SrTiO_3$ (single-crystalline target) or $SrRuO_3$ (sintered powder from Praxair electronics), respectively. Using a continuous stream of O_2 gas, the vacuum chamber ($P_{base} < 1 \times 10^{-6}$ mbar) was brought to a pressure of $P = 0.080$ mbar after which the targets were pre-ablated (at 5 Hz for 6 min) to remove possible surface contaminations. The resistive heater was then placed in deposition position (directly facing the target at a distance of 5 cm) and heated to 700 °C at 50 °C min^{-1} (controlled by a thermocouple inside the heater). For deposition of $SrTiO_3$ the pressure was reduced to $P = 0.010$ mbar, whereas $SrRuO_3$ was deposited at the same pressure as used during preablation. In general, $SrTiO_3$ was deposited for 10 min and $SrRuO_3$ for 20 min, in the course of which both targets were ablated at 1 Hz. After deposition, the samples were cooled in 100 mbar O_2 at a maximum rate of 20 °C min^{-1} (Figure 10e).

Analysis and Characterization: Measurements were conducted before and after PLD by AFM (Dimension Icon from Bruker). To determine the relative surface coverage of nanosheets, at least five different areas were scanned whereupon a value was obtained by image analysis software (ImageJ 1.46r). XRR and diffraction were performed either on an X'pert PRO MRD or an X'pert PRO Powder diffractometer (from PANalytical) both equipped with a Göbel mirror and a PIXcel detector (3D in the case of the MRD; 1D in the case of the Powder). In addition, a four-bounce Ge(220) monochromator was used on the MRD and for selected experiments the PIXcel^{3D} detector was replaced by a proportional counter with a triple axis module. For the films on nanosheets,ω was aligned on reflectance rather than the diffraction peak of the substrate. Lattice parameters were determined by fitting the different diffraction peaks with Gaussian functions, after which the Nelson–Riley function was used to determine the expected values and errors. High-resolution scanning electron microscopy was performed on a field emission microscope (Merlin from Zeiss) capable of in-lens secondary electron (SE) and energy selective backscattered (EsB) detection and additionally equipped with an angle selective backscatter (AsB) detector (NordlysNano from Oxford Instruments). EBSD was performed using a probe current of 250 pA and 4 × 4 binning and resulting Kikuchi patterns were fit to a cubic unit cell (P_{m3m}; a_c = 3.928 Å) using refined indexing (Aztec 2.2). Characterization was performed using a Physical Properties Measurement System (PPMS by Quantum Design) equipped with a vibrating sample magnetometer (VSM). Resistance was measured using a probe current of 1 μA, at which a resistance in the kΩ range was measured for the native Si substrate (in contrast to the thin films, the resistance of the substrate was of non-ohmic origin). Before conducting magnetization measurements, the samples were cut using a wafering blade (Isomet, Buehler) to fit in the pick-up coil, and their backsides were polished to remove possible magnetic contaminations. Magnetization was studied by a modified Sagnac interferometer as well, with which the out-of-plane magnetization was mapped by making use of the polar magneto-optic Kerr effect (MOKE).[26]

Supporting Information

Supporting Information is available from the Wiley Online Library or from the author.

Acknowledgements

The authors thank Tom Wijnands for performing X-ray photoelectron spectroscopy measurements. Financial support from the Chemical Sciences division of the Netherlands Organization for Scientific Research (NWO-CW) in the framework of the TOP program is gratefully acknowledged. The development of the Sagnac microscope is supported by NSF grant (ECCS-1346603) and Sloan Research Fellowship (BR2013-116).

Received: April 13, 2015
Revised: June 16, 2015
Published online: July 14, 2015

[1] A. Garg, Z. H. Barber, M. Dawber, J. F. Scott, A. Snedden, P. Lightfoot, *Appl. Phys. Lett.* **2003**, *83*, 2414.
[2] A. Ohtomo, H. Y. Hwang, *Nature* **2004**, *427*, 423.
[3] H. N. Lee, H. M. Christen, M. F. Chisholm, C. M. Rouleau, D. H. Lowndes, *Nature* **2005**, *433*, 395.
[4] H. Zheng, Q. Zhan, F. Zavaliche, M. Sherburne, F. Straub, M. P. Cruz, L. Q. Chen, U. Dahmen, R. Ramesh, *Nano Lett.* **2006**, *6*, 1401.
[5] E. Bousquet, M. Dawber, N. Stucki, C. Lichtensteiger, P. Hermet, S. Gariglio, J. M. Triscone, P. Ghosez, *Nature* **2008**, *452*, 732.
[6] J. Mannhart, D. G. Schlom, *Science* **2010**, *327*, 1607.
[7] S. A. Chambers, *Adv. Mater.* **2010**, *22*, 219.
[8] J. Ma, J. Hu, Z. Li, C. W. Nan, *Adv. Mater.* **2011**, *23*, 1062.
[9] A. Brataas, A. Kent, H. Ohno, *Nat. Mater.* **2012**, *11*, 372.
[10] A. Brataas, G. Bauer, P. Kelly, *Phys. Rep.* **2006**, *427*, 157.
[11] K. Kikuta, K. Noda, S. Okumura, T. Yamaguchi, S. Hirano, *J. Sol-Gel Sci. Technol.* **2007**, *42*, 381.
[12] T. Shibata, K. Fukuda, Y. Ebina, T. Kogure, T. Sasaki, *Adv. Mater.* **2008**, *20*, 231.
[13] H. Tetsuka, H. Takashima, K. Ikegami, H. Nanjo, T. Ebina, F. Mizukami, *Chem. Mater.* **2009**, *21*, 21.
[14] T. Shibata, Y. Ebina, T. Ohnishi, K. Takada, T. Kogure, T. Sasaki, *Cryst. Growth Des.* **2010**, *10*, 3787.
[15] M. Nijland, S. Kumar, R. Lubbers, D. H. A. Blank, G. Rijnders, G. Koster, J. E. ten Elshof, *ACS Appl. Mater. Interfaces* **2014**, *6*, 2777.
[16] T. Shibata, H. Takano, Y. Ebina, D. S. Kim, T. C. Ozawa, K. Akatsuka, T. Ohnishi, K. Takada, T. Kogure, T. Sasaki, *J. Mater. Chem. C* **2014**, *2*, 407.
[17] K. Taira, Y. Hirose, S. Nakao, N. Yamada, T. Kogure, T. Shibata, T. Sasaki, T. Hasegawa, *ACS Nano* **2014**, *8*, 6145.
[18] V. Nicolosi, M. Chhowalla, M. G. Kanatzidis, M. S. Strano, J. N. Coleman, *Science* **2013**, *340*, 1226419.
[19] A. Callaghan, C. W. Moeller, R. Ward, *Inorg. Chem.* **1966**, *5*, 1572.
[20] G. Koster, L. Klein, W. Siemons, G. Rijnders, J. S. Dodge, C. B. Eom, D. H. A. Blank, M. R. Beasley, *Rev. Mod. Phys.* **2012**, *84*, 253.
[21] Q. Gan, R. A. Rao, C. B. Eom, J. L. Garrett, M. Lee, *Appl. Phys. Lett.* **1998**, *72*, 978.
[22] K. Terai, T. Ohnishi, M. Lippmaa, H. Koinuma, M. Kawasaki, *Jpn. J. Appl. Phys.* **2004**, *43*, L227.
[23] C. U. Jung, H. Yamada, M. Kawasaki, Y. Tokura, *Appl. Phys. Lett.* **2004**, *84*, 2590.
[24] Y. Ebina, T. Sasaki, M. Watanabe, *Solid State Ionics* **2002**, *151*, 177.
[25] T. Tanaka, Y. Ebina, K. Takada, K. Kurashima, T. Sasaki, *Chem. Mater.* **2003**, *15*, 3564.
[26] J. Xia, P. T. Beyersdorf, M. M. Fejer, A. Kapitulnik, *Appl. Phys. Lett.* **2006**, *89*, 062508.